# Influence of cerium precursors on the structure and reducibility of mesoporous CuO-CeO$_2$ catalysts for CO oxidation

Lei Qi [a], Qiang Yu [a], Yue Dai [a], Changjin Tang [a], Lianjun Liu [a], Hongliang Zhang [a], Fei Gao [b,**], Lin Dong [a,b,*], Yi Chen [a]

[a] Key Laboratory of Mesoscopic Chemistry of MOE, School of Chemistry and Chemical Engineering, Nanjing University, Nanjing 210093, PR China
[b] Jiangsu Key Laboratory of Vehicle Emissions Control, Center of Modern Analysis, Nanjing University, Nanjing 210093, PR China

## ARTICLE INFO

## ABSTRACT

This work investigated the effects of cerium precursors [Ce(NO$_3$)$_3$ and (NH$_4$)$_2$Ce(NO$_3$)$_6$] on the structure, surface state, reducibility and CO oxidation activity of mesoporous CuO-CeO$_2$ catalysts. The catalysts were characterized by TG–DTA, XRD, LRS, N$_2$ adsorption–desorption, HRTEM, XPS, H$_2$-TPR and in situ FT-IR. The obtained results suggested that the precursors exerted a great influence on the properties of CuO-CeO$_2$ catalysts: (1) compared with the catalysts from Ce(III) precursor, the derived Ce(IV) precursor catalysts showed smaller grain size, higher BET surface area, narrower pore size distribution, whereas their reducibility and activities were not enhanced. (2) In contrast, the catalysts from Ce(III) precursor without excellent texture displayed high reducibility and activities for CO oxidation due to the high content of Ce$^{3+}$, following the redox equilibrium of Cu$^{2+}$ + Ce$^{3+}$ ↔ Cu$^+$ + Ce$^{4+}$ shifting to right to form more stable Cu$^+$ species, which was the origin of synergistic effect. The synergistic effect between copper and cerium was the predominant contributor to the improved catalytic activities of CuO-CeO$_2$ catalysts, instead of structural properties.

© 2012 Elsevier B.V. All rights reserved.

## 1. Introduction

In recent years, ceria (CeO$_2$) has been received increasing attentions and found tremendous applications in environmental catalysis due to its high oxygen storage-release capacity associated with Ce$^{4+}$/Ce$^{3+}$ redox cycle [1,2]. It was well documented that the catalytic activities of ceria-based catalysts were greatly promoted not only by precious metals, but also by base metals, particularly copper species [3–6]. For instance, CuO-CeO$_2$ catalysts had been shown to be very active for CO oxidation, exhibiting specific activities comparable with or even superior to precious metal catalysts [7,8].

In principle, the high activity of CuO-CeO$_2$ is correlated with the synergism of copper–ceria interactions, which facilitates the electron exchanges between Cu$^{2+}$/Cu$^+$ and Ce$^{3+}$/Ce$^{4+}$, with both components being significantly more readily reduced or oxidized than the corresponding independent ones [9–11]. The redox cycles between Cu$^{2+}$ and Cu$^+$ (and concomitantly Ce$^{4+}$ and Ce$^{3+}$) are often regarded as the key steps of the reaction mechanism of CO oxidation

and consequently, as well as in determining the catalytic behavior [12]. Thus, the CuO-CeO$_2$ catalysts with facile electron exchanges can easily form Cu$^+$ species for CO adsorption, which is an important factor to promote activity of CO oxidation [13]. Another important factor is the presence of the oxygen vacancy provided by CeO$_2$, which can in turn generate active oxygen for the reaction [14]. Other than these, unique texture of ceria-based catalysts is also advantageous for their catalytic performances. For example, mesoporous CuO-CeO$_2$ catalysts had been reported to display superior activity toward CO oxidation in comparison with usually used CuO/CeO$_2$ catalysts [15–17]. Consequently, controllable synthesis of mesoporous CuO-CeO$_2$ catalysts, which possess facile redox process and a high concentration of oxygen vacancies, will be beneficial to the enhancement of activity toward CO oxidation.

Until now, Ce(NO$_3$)$_3$ and (NH$_4$)$_2$Ce(NO$_3$)$_6$ are two of the most widely used precursors to synthesize CuO-CeO$_2$ catalysts. Tang et al. [18] prepared CuO-CeO$_2$ catalysts by precipitation method and used Ce(NO$_3$)$_3$ as cerium precursor. They pointed out that the discrepancies in the dispersion of copper species and the degree of interaction between copper species and ceria determined the reversible redox properties, and consequently the catalytic performance of CO oxidation. Li et al. [19] obtained CuO-CeO$_2$ catalysts from (NH$_4$)$_2$Ce(NO$_3$)$_6$ by urea co-precipitation–gelation method. They found that the reducibility of ceria was promoted by the addition of copper, leading to the significantly enhanced activity in the water–gas shift reaction (WGS). However, to our knowledge,

* Corresponding author at: School of Chemistry and Chemical Engineering, Nanjing University, Hankou Road 22#, Nanjing, Jiangsu 210093, China. Tel.: +86 25 83592290; fax: +86 25 83317761.
** Corresponding author. Tel.: +86 25 83592290; fax: +86 25 83317761.
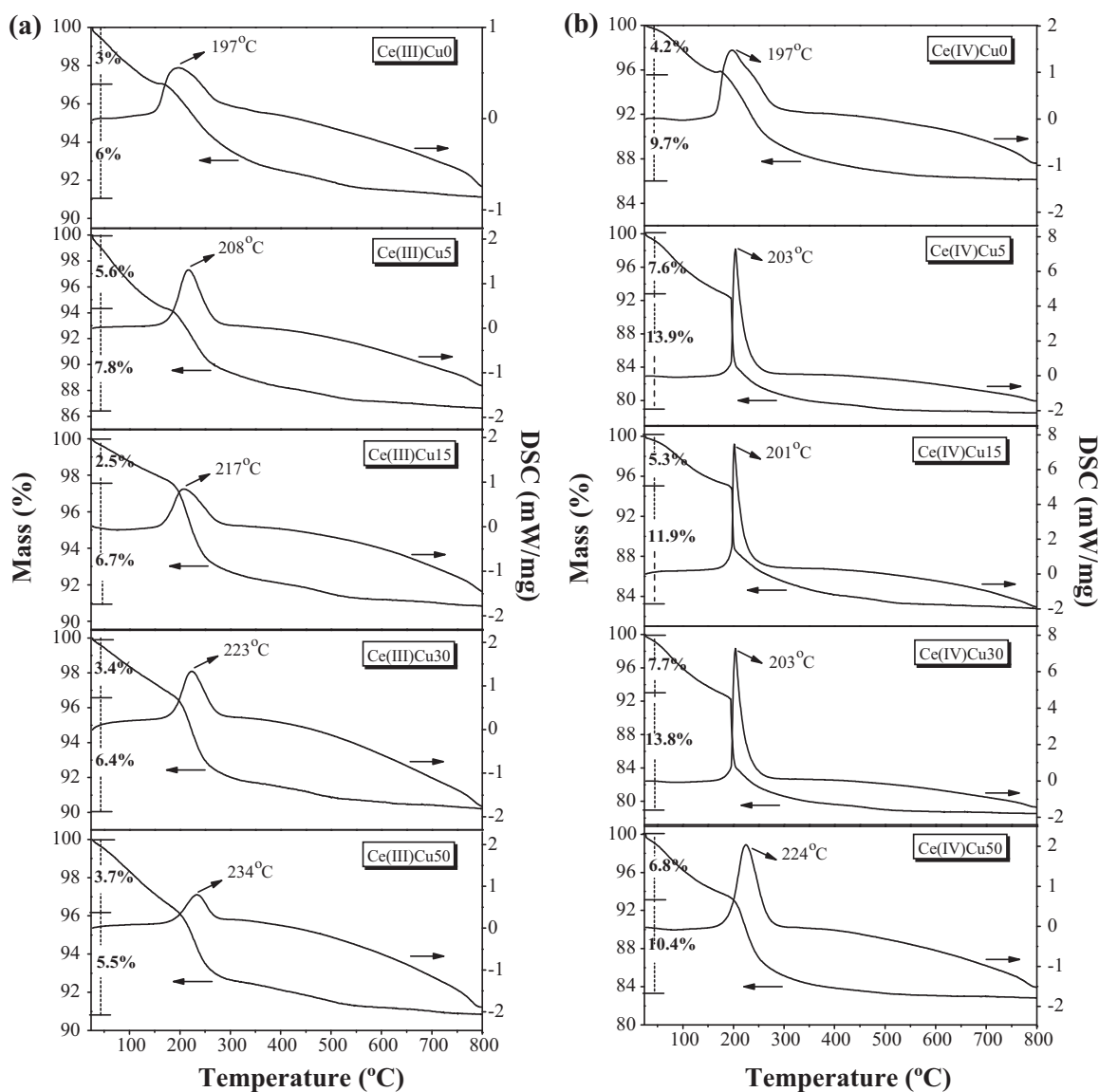*E-mail addresses:* gaofei@nju.edu.cn (F. Gao), donglin@nju.edu.cn (L. Dong).

**Fig. 1.** TG–DTA curves of the uncalcinated samples: (a) Ce(III)Cu$x$; (b) Ce(IV)Cu$x$.

little attention has been paid to comparing the effect of cerium precursors on the structure, surface state, redox property and CO oxidation activity of mesoporous CuO-CeO$_2$ catalysts. On the other hand, previous researches proved that many factors could influence the activity of CuO-CeO$_2$ catalysts, such as surface area, porous structure [15], synergistic effect between copper and cerium [12], oxygen vacancy [14], etc. Nevertheless, the contributions of these factors to the catalytic activity and the predominant contributor to the enhanced activity are still not clear.

In this work, a series of mesoporous CuO-CeO$_2$ catalysts were prepared by a surfactant-assisted co-precipitation method and characterized by means of TG–DTA, XRD, LRS, N$_2$ adsorption–desorption, HRTEM, H$_2$-TPR, in situ FT-IR and CO oxidation model reaction. The studies have mainly focused on (1) exploring the influence of cerium precursors (i.e. Ce(NO$_3$)$_3$ or (NH$_4$)$_2$Ce(NO$_3$)$_6$) on the structure, surface state, reduction property and CO oxidation activity of CuO-CeO$_2$ catalysts; (2) investigating the contribution of structural property and synergistic effect to the reducibility and catalytic activity of CO oxidation, and deciding the major contributor to improve the activity.

## 2. Experimental

### 2.1. Catalyst preparation

All chemicals were of analytical grade and used as received without further purification. CuO-CeO$_2$ catalysts with different Cu contents were synthesized by a surfactant-assisted co-precipitation method. In a typical synthesis procedure, 6 mmol cetyltrimethyl ammonium bromide (CTAB) was dissolved in 200 mL distilled water at room temperature, followed by the addition of 10 mmol Ce(NO$_3$)$_3$·6H$_2$O or (NH$_4$)$_2$Ce(NO$_3$)$_6$ and a calculated amount of Cu(NO$_3$)$_2$·3H$_2$O. After that, an aqueous solution of NaOH (0.2 mol L$^{-1}$) was added dropwise to the pre-mixed solution under vigorous stirring until pH 9. The obtained suspension was aged at 90 °C for 3 h. The precipitate was filtered, washed and dried at 110 °C for 12 h. Subsequently, the resultant powders were calcined at 400 °C for 5 h in air. The catalysts were denoted as Ce(III)Cu$x$ or Ce(IV)Cu$x$, where $x$ stands for the percentage of Cu/(Cu + Ce) molar ratio. The nominal contents of Cu were 0, 5, 15, 30 and 50 mol%, respectively.

**Table 1**
Chemical composition, grain size, lattice parameter, full width at half maximum (FWHM) of $F_{2g}$ vibration band, the area ratio of Raman bands at 590 and 460 cm$^{-1}$, surface area, pore size, pore volume and $H_2$ consumption of CuO-CeO$_2$ catalysts.

| Catalysts | Cu (mol%)[a] | Cu/Ce[b] | Cu/Ce[c] | $D$ (nm)[d] | $a$ (nm)[e] | FWHM (cm$^{-1}$)[f] | $A_{590}/A_{460}$[g] | $S_{BET}$ (m$^2$ g$^{-1}$)[h] | $r$ (nm)[i] | $V$ (cm$^3$ g$^{-1}$)[j] | Theoretical $H_2$ consumption (µmol g$^{-1}$) | Actual $H_2$ consumption (µmol g$^{-1}$) |
|---|---|---|---|---|---|---|---|---|---|---|---|---|
| Ce(III)Cu0 | 0 | 0 | 0 | 9.5 | 0.5427 | 33 | 0.05 | 143 | 8.37 | 0.30 | – | – |
| Ce(III)Cu5 | 5.51 | 0.06 | 0.20 | 8.1 | 0.5423 | 35 | 0.22 | 130 | 7.20 | 0.23 | 327.6 | 789.3 |
| Ce(III)Cu15 | 12.99 | 0.15 | 0.33 | 7.8 | 0.5418 | 50 | 0.23 | 149 | 8.59 | 0.32 | 835.4 | 1397.0 |
| Ce(III)Cu30 | 28.10 | 0.39 | 0.64 | 6.6 | 0.5414 | 47 | 0.15 | 137 | 11.88 | 0.41 | 1874.9 | 2219.6 |
| Ce(III)Cu50 | 51.63 | 1.07 | 0.95 | 5.2 | 0.5424 | 41 | 0.16 | 123 | 9.73 | 0.30 | 4140.4 | 4152.1 |
| Ce(IV)Cu0 | 0 | 0 | 0 | 5.0 | 0.5431 | 32 | 0.02 | 177 | 4.10 | 0.18 | – | – |
| Ce(IV)Cu5 | 5.68 | 0.06 | 0.15 | 4.2 | 0.5428 | 37 | 0.04 | 218 | 3.72 | 0.20 | 337.7 | 1000.3 |
| Ce(IV)Cu15 | 14.31 | 0.17 | 0.34 | 4.1 | 0.5430 | 52 | 0.14 | 214 | 3.73 | 0.20 | 892.1 | 1407.7 |
| Ce(IV)Cu30 | 31.58 | 0.46 | 0.62 | 3.9 | 0.5392 | 47 | 0.10 | 179 | 3.89 | 0.17 | 2200.0 | 2383.0 |
| Ce(IV)Cu50 | 52.08 | 1.09 | 0.94 | 3.7 | 0.5423 | 41 | 0.11 | 166 | 5.80 | 0.24 | 4170.6 | 4188.0 |

[a] Actual Cu content (mol%) determined by XRF.
[b] Actual atomic ratio (Cu/Ce) determined by XRF.
[c] Surface atomic ratio (Cu/Ce) determined by XPS.
[d] Grain size of CeO$_2$ determined from the XRD diffraction peak by Scherrer equation.
[e] Lattice parameter calculated from characteristic XRD peaks of CeO$_2$ by Bragg's law.
[f] FWHM calculated from the characteristic peak of CeO$_2$ ($F_{2g}$) in Raman spectra.
[g] The area ratio of Raman bands at 590 and 460 cm$^{-1}$.
[h] Surface area determined from BET equation.
[i] Average pore radius determined from BJH method.
[j] Pore volume.

## 2.2. Catalyst characterization

Thermogravimetry and differential thermal analysis (TG–DTA) of the catalysts was carried out on a Netzsch thermoanalyzer STA 449C with a heating rate of 10 °C min$^{-1}$ in a flowing air.

The actual Cu contents in these CuO-CeO$_2$ catalysts were analyzed by X-ray fluorescence spectrometer (ARL-9800).

X-ray diffraction (XRD) patterns were recorded on a Philips X'pert Pro diffractometer using Ni-filtered Cu Kα radiation (0.15418 nm). The X-ray tube was operated at 40 kV and 40 mA.

Laser Raman spectroscopy (LRS) analysis was performed on a Jobin-Yvon (France-Japan) T64000 type Laser Raman spectroscopy using Ar$^+$ laser beam. The Raman spectra were recorded with an excitation wavelength of 514 nm and the laser power of 300 mW.

The surface areas of the catalysts were determined via nitrogen adsorption at −196 °C with the Brunauer–Emmet–Teller (BET) method using a Micrometrics ASAP-2020 adsorption apparatus. The pore size distribution was calculated from the desorption branch of the N$_2$ isotherm by using the Barrett–Joyner–Halenda (BJH) algorithm. Prior to each measurement, the sample was pretreated at 300 °C for 4 h under vacuum.

High resolution transmission electron microscope (HRTEM) investigations were carried out using a JEM-2100 instrument at an acceleration voltage of 200 kV.

X-ray photoelectron spectroscopy (XPS) analysis was performed on a PHI5000 VersaProbe high performance electron spectrometer, using monochromatic Al Kα radiation (1486.6 eV) operating at an accelerating voltage of 15 kV. All binding energies (BE) were referenced to the adventitious C1s at 284.6 eV. This reference gave BE values with an accuracy at ±0.1 eV.

H$_2$ temperature-programmed reduction (H$_2$-TPR) experiments were carried out in a quartz U-tube reactor connected to a thermal conduction detector with 7.3% H$_2$/Ar as reductant. 50 mg sample was used for each measurement. Before reduction, the sample was pretreated in a N$_2$ stream at 200 °C for 1 h and then cooled to room temperature. After that, H$_2$/Ar mixture was switched on and the sample was heated with a heating rate of 10 °C min$^{-1}$. The overlapped peaks were deconvoluted fitting with Gaussian–Lorentzian curves using the attached tool of origin PFM (Peak Fitting Module).

In situ Fourier transform infrared spectroscopy (FT-IR) was collected from 1000 to 4000 cm$^{-1}$ with a resolution 4 cm$^{-1}$ on a Nicolet 5700 FT-IR instrument (Thermo Electron Corporation, USA), using 64 scans per spectrum. The CuO-CeO$_2$ catalyst (about 10 mg) was pressed into a thin self-supporting wafer and mounted inside a high temperature cell (HTC-3, Harrick Scientific Corporation, USA). The wafer was pretreated for 1 h at 200 °C in the flowing N$_2$ atmosphere. After cooled to room temperature, the sample was conducted to a controlled stream of 2% CO/N$_2$ or a mixture of 2% CO/N$_2$ and pure O$_2$ for 30 min. In situ CO adsorption and CO and O$_2$ co-adsorption FT-IR spectra were recorded at various target temperatures with subtraction of the corresponding background reference.

## 2.3. Catalytic activity measurements

The CO oxidation activities of the catalysts were measured in a flow micro-reactor with a gas composition of 1.6 vol% CO, 20.8 vol% O$_2$ and 77.6 vol% N$_2$ at a space velocity of 30,000 mL g$^{-1}$ h$^{-1}$, and 50 mg catalyst was used for each measurement. The catalyst was pretreated in a N$_2$ stream at 200 °C for 1 h and then cooled to room temperature, after that, the mixed gases were switched on. Two columns and thermal conductivity detector (TCD) were used for the purpose of analyzing the production, column A with 13× molecular sieve for separating O$_2$, N$_2$ and CO, and column B, packed with Porapak Q for separating CO$_2$.

## 3. Results and discussion

### 3.1. TG–DTA results

As shown in the TG–DTA curves (Fig. 1), the processes of weight loss are similar and can be divided into two steps for all samples. The initial weight loss below 180 °C (denoted as step I) can be attributed to the desorption of water and condensation of hydroxyl groups [20]. The main weight loss is observed between 180 and 400 °C (denoted as step II), accompanying with a strong exothermic peak, which can be primarily assigned to the decomposition of the surfactant and the combustion of carbon species [21]. Moreover, the weight loss for step I and II of Ce(IV)Cu$x$ samples are higher than the corresponding step of Ce(III)Cu$x$ ones with the same copper contents. These results indicate that (NH$_4$)$_2$Ce(NO$_3$)$_6$ precursor can combine with more hydroxyl and CTAB than Ce(NO$_3$)$_3$ precursor during the synthesis process. As a matter of fact, the tetravalent ceric ion formed in the ammonium cerium nitrate aqueous solution
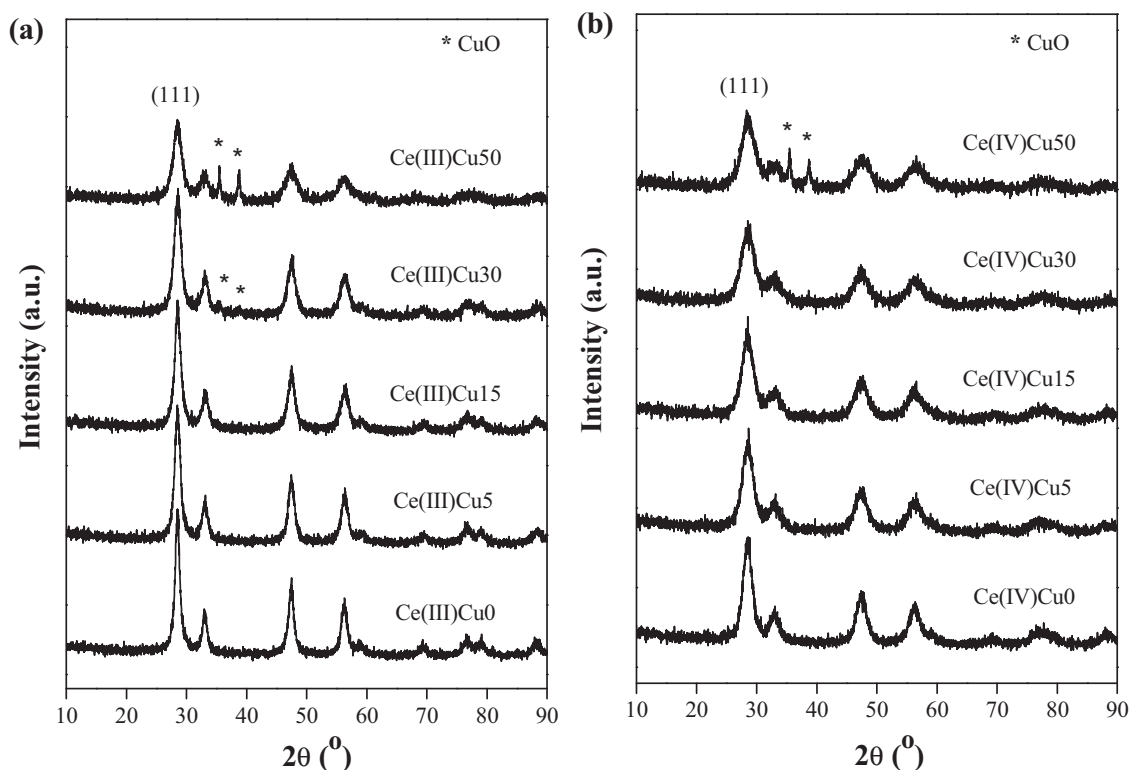
**Fig. 2.** XRD patterns of CuO-CeO$_2$ catalysts with different Cu contents: (a) Ce(III)Cu*x*; (b) Ce(IV)Cu*x*.

(Ce(NO$_3$)$_6$$^{2-}$) is actually a stable 12-coordinate icosahedron complex on which each NO$_3$$^-$ ligand is bounded to Ce$^{4+}$ in its chelate mode by two oxygen atoms [22]. Cerium(IV) is, thus, present in solution as an anionic complex, while cerium(III) is present as a hydrolyzed cation [22]. This difference in charge would benefit the proximity of anionic Ce(NO$_3$)$_6$$^{2-}$ and the cationic copper (Cu$^{2+}$) as well as positive electric surfactant (CH$_3$(CH$_2$)$_{15}$N$^+$(CH$_3$)$_3$) through an electrostatic adsorption mechanism. This hypothesis is also supported by XRF results (Table 1) that the actual Cu contents of Ce(IV)Cu*x* samples are higher than those of Ce(III)Cu*x* ones with the same nominal Cu contents.

### 3.2. Structure characterization (XRD, LRS, N$_2$ adsorption–desorption, HRTEM)

#### 3.2.1. XRD and LRS results

Fig. 2 shows XRD patterns of Ce(III)Cu*x* and Ce(IV)Cu*x* samples. As shown in Fig. 2(a), no typical diffraction peaks of crystalline CuO can be observed for Ce(III)Cu5 and Ce(III)Cu15 samples, indicating the existence of well dispersion of CuO species on the surface of CeO$_2$, or/and the incorporation of copper into the CeO$_2$ lattice [23]. As Cu content reaches 30 and 50 mol%, the XRD peaks of crystalline CuO ($2\theta = 35.5°$, $38.7°$) [JCPDS (Card No. 41-0254)] appear



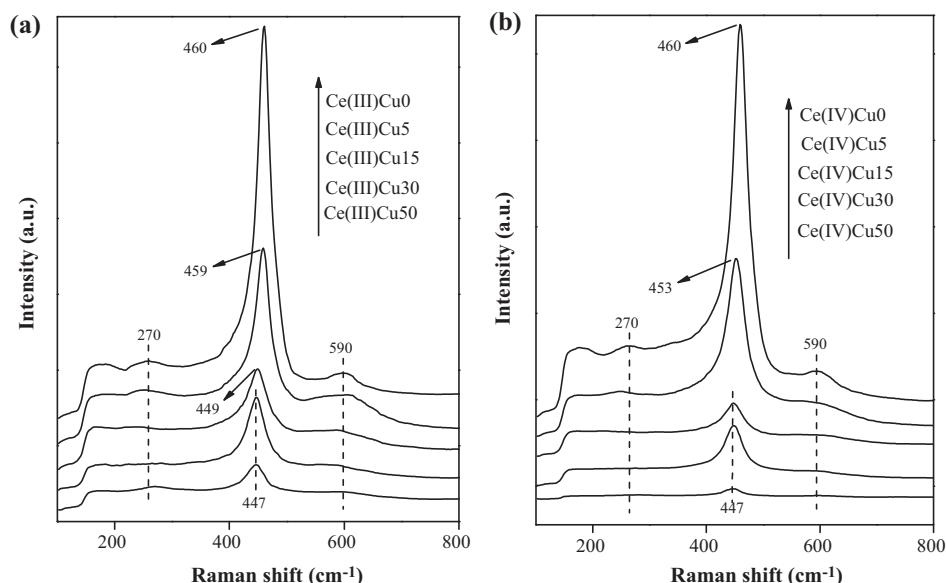**Fig. 3.** Raman spectra of CuO-CeO$_2$ catalysts with different Cu contents: (a) Ce(III)Cu*x*; (b) Ce(IV)Cu*x*.
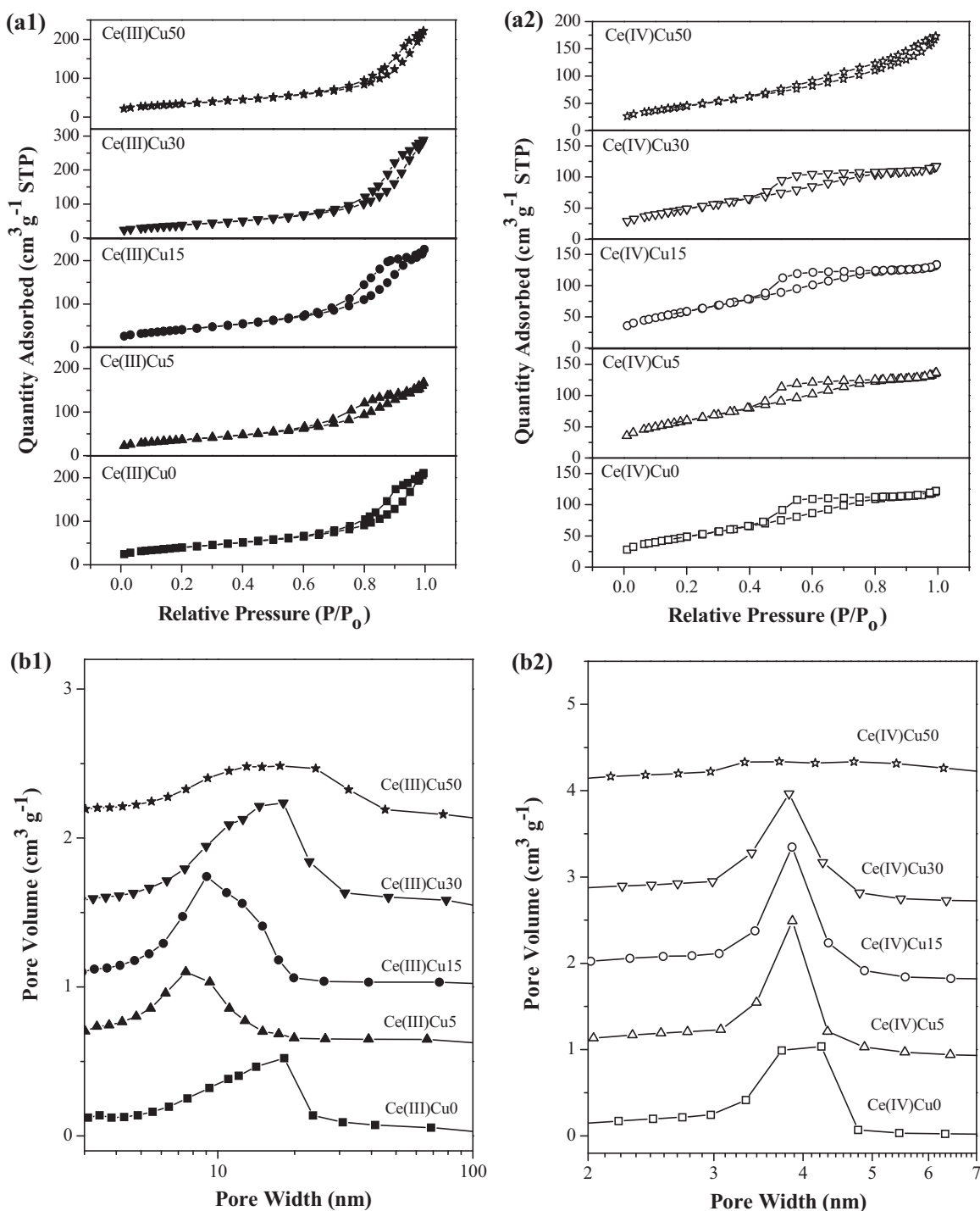
**Fig. 4.** $N_2$ adsorption–desorption isotherms (a1, a2) and the corresponding distribution curves of pore size (b1, b2) of CuO-CeO$_2$ catalysts with different Cu contents.

and their intensities increase with the Cu contents. In Fig. 2(b), for Cu content below 50 mol%, only the diffraction peaks of cubic CeO$_2$ with fluorite structure [JCPDS (Card No. 34-0394)] can be observed for Ce(IV)Cu$x$ samples. Once Cu content increases to 50 mol%, the characteristic peaks of crystalline CuO appear.

The grain size and lattice parameter of the oxides before and after copper incorporation are summarized in Table 1. The grain size of Ce(III)Cu$x$ is bigger than that of Ce(IV)Cu$x$ with the same Cu contents, and all of them gradually decrease with the introduction of more amount of copper species. The lattice parameters of cubic CeO$_2$ slightly decrease after the addition of copper species,

which provides evidence that some $Cu^{2+}$ ions are incorporated into ceria lattice, probably forming Cu–O–Ce species, by considering that the radius of $Cu^{2+}$ ion (0.073 nm) is smaller than that of $Ce^{3+}$ (0.110 nm) or $Ce^{4+}$ ion (0.097 nm) [24]. Additionally, the lattice parameter observed in some case of these samples appears higher than that typically observed for pure CeO$_2$ (0.5409 nm) [25], which is possibly due to the higher content of $Ce^{3+}$ in these samples than in the reported one, as confirmed by XPS results discussed below.

Raman spectra of the studied samples are shown in Fig. 3. Ce(III)Cu0 and Ce(IV)Cu0 samples exhibit the characteristic $F_{2g}$ vibration band at 460 cm$^{-1}$ [26]. Once copper species is introduced,
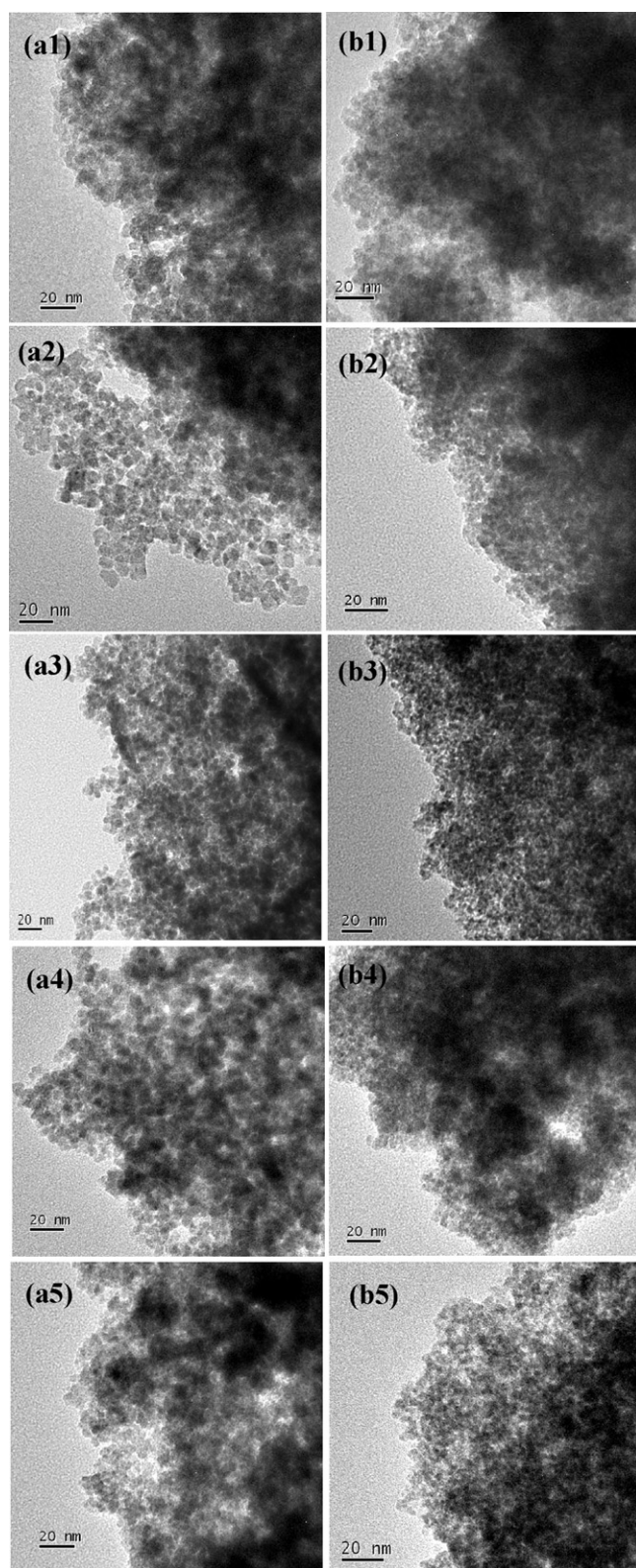
**Fig. 5.** TEM images of (a1) Ce(III)Cu0, (a2) Ce(III)Cu5, (a3) Ce(III)Cu15, (a4) Ce(III)Cu30, (a5) Ce(III)Cu50, (b1) Ce(IV)Cu0, (b2) Ce(IV)Cu5, (b3) Ce(IV)Cu15, (b4) Ce(IV)Cu30 and (b5) Ce(IV)Cu50.
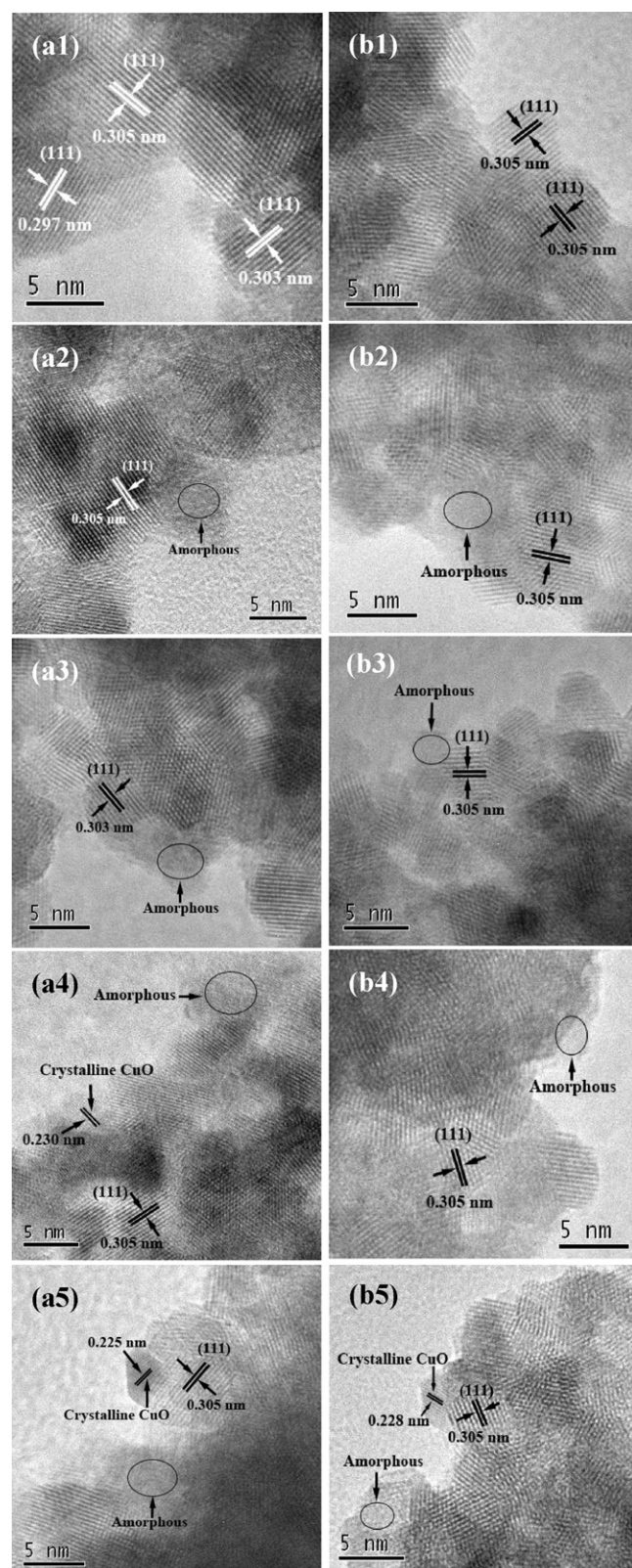
**Fig. 6.** HRTEM images of (a1) Ce(III)Cu0, (a2) Ce(III)Cu5, (a3) Ce(III)Cu15, (a4) Ce(III)Cu30, (a5) Ce(III)Cu50, (b1) Ce(IV)Cu0, (b2) Ce(IV)Cu5, (b3) Ce(IV)Cu15, (b4) Ce(IV)Cu30 and (b5) Ce(IV)Cu50.

this peak shifts from 460 to 447 cm$^{-1}$, and becomes broader and weaker. This shift may imply that changes in the lattice parameter with particle size have occurred, as it was previously reported that a change of the particle size of CeO$_2$ from 6 nm to 5 μm led to a shift in peak position about 10 cm$^{-1}$, and was well explained by phonon confinement model [27,28]. Another reason of shifting and broadening may be the presence of oxygen vacancies [29], which is related to structural defects derived from partially incorporation of copper into CeO$_2$ lattice, in agreement with the decrease of lattice parameter. Additionally, two weak bands at ca. 270 and 590 cm$^{-1}$ are attributed to oxygen vacancies, and the relative concentration of oxygen vacancies can be reflected by the ratio of $A_{590}/A_{460}$ [14] (Table 1). $A_{590}/A_{460}$ values of CuO-CeO$_2$ are higher than pure CeO$_2$,

indicating the formation of more oxygen vacancies with the incorporation of copper. Moreover, $A_{590}/A_{460}$ values of Ce(III)Cu$x$ are higher than those of Ce(IV)Cu$x$ with the same Cu contents, which is related to a higher concentration of oxygen vacancies in Ce(III)Cu$x$ samples. Thus, as implied from XRD and Raman results, Ce(IV) precursor promotes the formation of CuO-CeO$_2$ with smaller grain size, while Ce(III) precursor is beneficial to obtain CuO-CeO$_2$ with higher concentration of oxygen vacancies.

### 3.2.2. N$_2$ adsorption–desorption and TEM results

As shown in Fig. 4(a1) and (a2), all samples exhibit IV-type isotherms and H2-type hysteresis loops according to the IUPAC classification, typical for wormhole-like mesostructure and
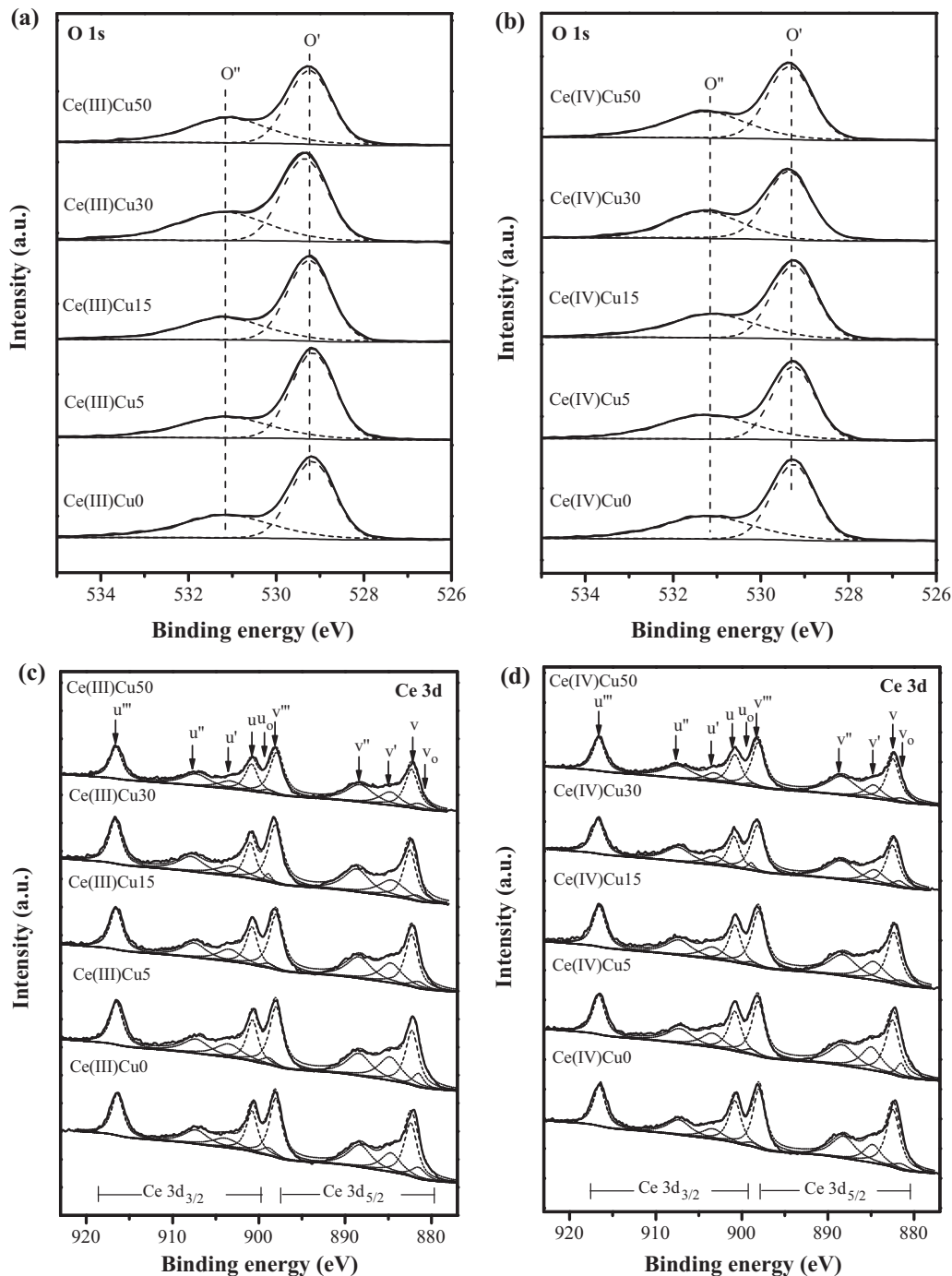


**Fig. 7.** XPS of CuO–CeO$_2$ catalysts: (a), (b) O1s; (c), (d) Ce 3d; (e),(f) Cu 2p; (g), (h) Cu LMM.
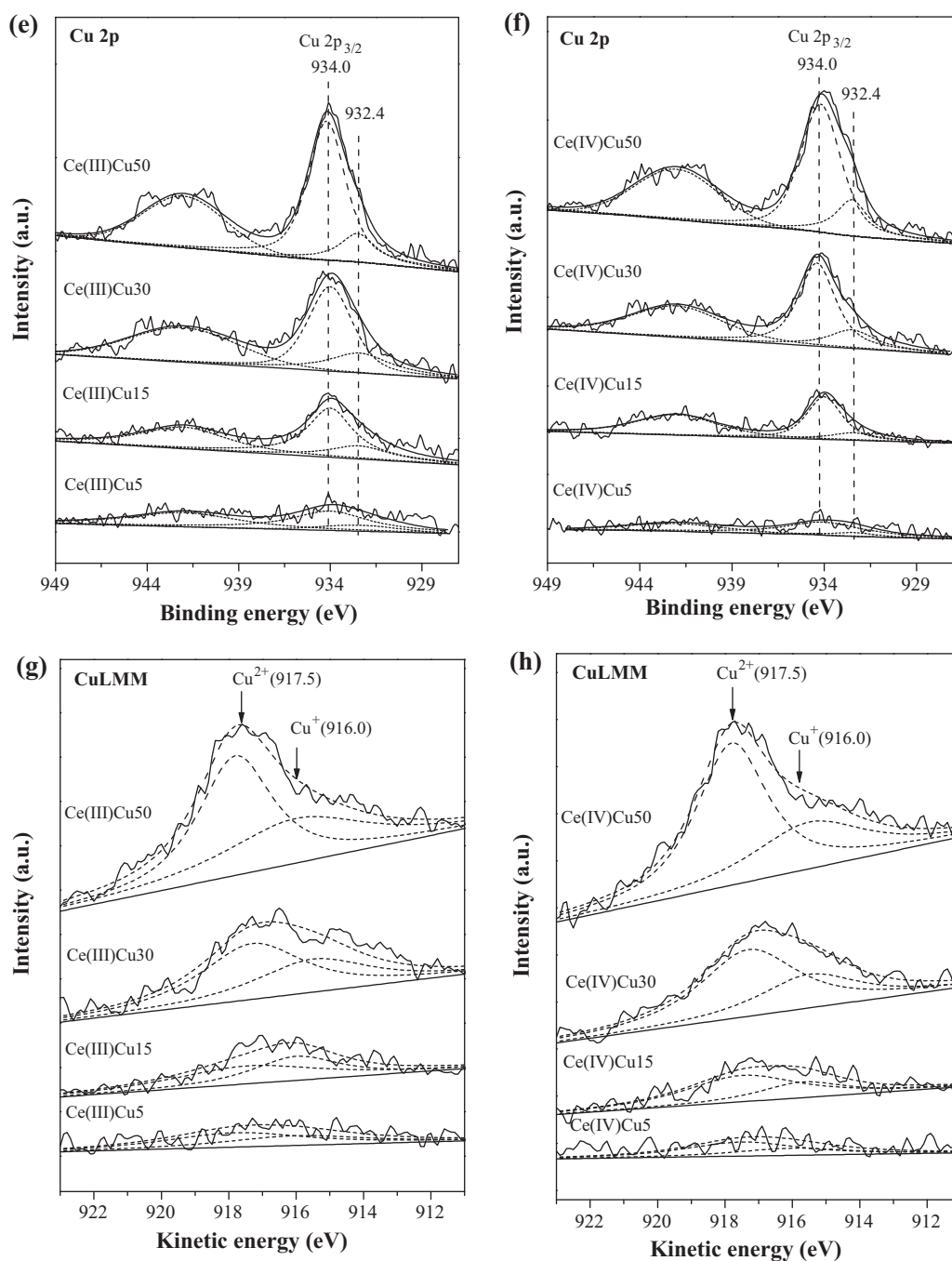
**Fig. 7.** (*continued*).

heterogeneously distributed mesoporous radii. The pore size distributions of Ce(III)Cu$x$ ($x \leq 30$) samples (5–30 nm) are much broader than those of Ce(IV)Cu$x$ ($x \leq 30$) ones (3–5 nm) (Fig. 4(b1) and (b2)). Ce(III)Cu50 and Ce(IV)Cu50 own pore size distributions in a wide range probably due to the destruct of pore structure by excessive crystalline CuO [23]. Additionally, Ce(IV)Cu$x$ samples exhibit higher BET surface area and smaller BJH pore size than those of Ce(III)Cu$x$ with the same Cu contents (Table 1).

Wormhole-like mesostructure, aggregated by metal oxide nanoparticles, can be directly observed for all samples in Fig. 5. The particle sizes of Ce(IV)Cu$x$ are around 3–4 nm, which are smaller than those of Ce(III)Cu$x$ (5–10 nm). Structural details of nanoparticles were obtained by HRTEM images in Fig. 6. All samples have the

spacing of lattice fringes around 0.297–0.305 nm, ascribed to the (1 1 1) crystallographic planes of CeO$_2$. In addition, amorphous surface CuO$x$, which are distributed on the top or at the edge of ceria crystal [30], are found for all CuO-CeO$_2$ samples. Besides, a few CuO crystallites with the lattice spacing 0.225–0.230 nm appear in Ce(III)Cu30, Ce(III)Cu50 and Ce(IV)50 samples. Combined with XRD and Raman results, CuO-CeO$_2$ catalysts with the lower copper oxide amount ($\leq$15 mol% for Ce(III)Cu$x$ and $\leq$30 mol% for Ce(IV)Cu$x$) contain two kinds of copper species: high dispersed CuO species and copper partially incorporation into CeO$_2$ lattice. Furthermore, catalysts with excess copper oxide (Ce(III)Cu30, Ce(III)Cu50 and Ce(IV)50 samples) include the third copper species: crystalline CuO.
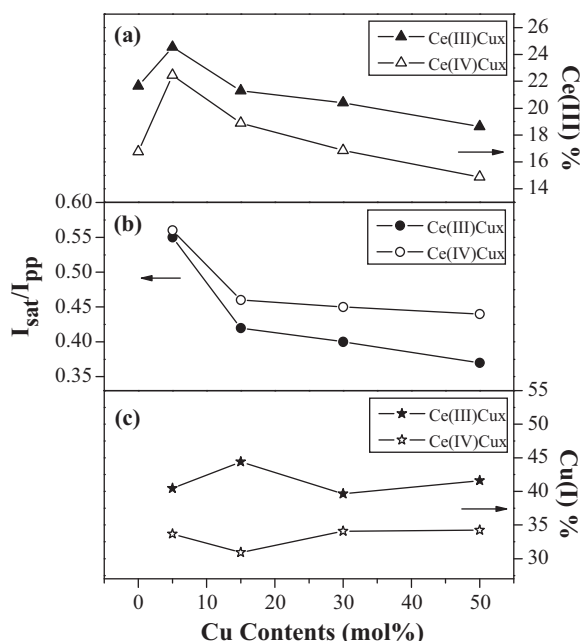
**Fig. 8.** (a) The relative area of the $u_0$ ($v_0$) and $u'$ ($v'$) peaks to the area of Ce 3d region (Ce(III)%) for CuO-CeO$_2$ catalysts; (b) the ratio of the intensities of Cu 2p satellite peaks to those of the principal peaks ($I_{sat}/I_{pp}$) for CuO-CeO$_2$ catalysts; (c) the ratio of Cu$^+$ peak area to the total area (Cu(I)%) for CuO-CeO$_2$ catalysts.

### 3.3. Chemical states of CuO-CeO$_2$ catalysts (XPS results)

XPS was performed in order to further illuminate the surface composition and the chemical state of the elements existing in CuO-CeO$_2$ catalysts. The surface atomic ratios of Cu/Ce (except Ce(III)Cu50 and Ce(IV)Cu50) determined by XPS are much higher than the corresponding Cu/Ce ratios determined by XRF (Table 1), indicating the enrichment of copper species on the catalysts surface. Fig. 7(a and b) shows the O1s spectra of CuO-CeO$_2$ catalysts. In addition to the presence of the main peak O' at 529.3 eV attributed to the lattice oxygen of the metal oxides, an apparent shoulder peak O'' at 531.2 eV representing the absorbed oxygen in hydroxyl and carbonate groups is observed [29].

The complex spectrum of Ce 3d is decomposed into ten components with the assignment defined in Fig. 7(c and d). The two sets of spin–orbital multiplets, corresponding to the 3d$_{3/2}$ and 3d$_{5/2}$ contributions, are labeled as $u$ and $v$, respectively. A favorable method, which considers the relative area of the $u_0$ ($v_0$) and $u'$ ($v'$) peaks to the area of Ce 3d region, is applied to estimate Ce$^{3+}$ content [31]:Ce(III)% = $\frac{100\times[S(u_0)+S(u')+S(v_0)+S(v')]}{\sum[S(u)+(v)]}$%

The Ce(III)% values for the two series of CuO-CeO$_2$ catalysts are reported in Fig. 8(a). It can be seen that there is a certain amount of Ce$^{3+}$ in all the catalysts, and that the Ce$^{3+}$ quantities of Ce(III)Cu$x$ samples are slightly higher than those of Ce(IV)Cu$x$ ones with the same Cu contents. Additionally, the values of Ce(III)% for these samples are much higher than that of pure CeO$_2$ reported in the literature (Ce(III)% = 6.75%) [25], which leads to the higher lattice parameters of these samples than that of the reported one.

Cu 2p spectra in Fig. 7(e and f) shows the principal peaks of Cu 2p$_{3/2}$ at about 934.0 eV and corresponding satellite peaks at 938–948 eV with shake-up structure. Additionally, a weak Cu 2p$_{3/2}$ peak centered at 932.4 eV can be observed. It is reported that the higher Cu 2p$_{3/2}$ binding energy and the shake-up peak are two major XPS characteristics of Cu$^{2+}$ species, while the lower Cu 2p$_{3/2}$ binding energy and absence of the shake-up peak are characteristic of reduced copper species [32]. Thus, most Cu species initially present in these samples are in divalent oxidation state and a

small amount in lower-valence state (Cu$^+$ and/or Cu$^0$). The reduced degree of Cu species can be investigated by determining the ratio of the intensities of the satellite peaks to those of the principal peaks ($I_{sat}/I_{pp}$, Fig. 8(b)) [10]. Due to the photoreduction in the spectrometer, it is difficult to estimate the accurate reduction degree of Cu species, but this method gives valuable information for comparison between these two series samples [10]. After the comparison between bulk CuO ($I_{sat}/I_{pp}$ = 0.57) and these samples, a slightly reduced copper phase is observed for all samples. Moreover, the $I_{sat}/I_{pp}$ values for Ce(III)Cu$x$ are lower than those for Ce(IV)Cu$x$, indicating the appearance of more amount of low-valence copper species in Ce(III)Cu$x$ samples. In order to clarify the low valence state of copper species, Auger Cu LMM lines were also investigated over these mentioned catalysts, as shown in Fig. 7(g and h). It can be observed that the reduced copper species mainly exist as Cu$^+$ (916.0 eV) [33]. As shown in Fig. 8(c), the ratios of Cu$^+$ area to the total area (denoted as Cu(I)%) for Ce(III)Cu$x$ samples are higher than those for Ce(IV)Cu$x$, suggesting more amount of Cu$^+$ species in Ce(III)Cu$x$ samples.

As discussed above, Ce(III)Cu$x$ samples contain more amount of Ce$^{3+}$ (Ce(III)%) and Cu$^+$ ($I_{sat}/I_{pp}$, Cu(I)%) species than Ce(IV)Cu$x$ ones, which are expected to exhibit different reduction properties and CO oxidation activities subsequently. Nevertheless, there is more information that can be obtained from Fig. 8(a and b). The ratios of Ce$^{3+}$ and Cu$^{2+}$ in CuO-CeO$_2$ catalysts decrease simultaneously as more amount of Cu species incorporation. These results provide unambiguous evidence of existence of redox equilibrium of Cu$^{2+}$ + Ce$^{3+}$ ↔ Cu$^+$ + Ce$^{4+}$, which has been claimed to be the source of a synergistic interaction between copper and ceria species in the CuO-CeO$_2$ catalysts. Furthermore, the ratios of Ce$^{3+}$ and Cu$^{2+}$ in Ce(III)Cu$x$ samples decline in a higher degree than those in Ce(IV)Cu$x$ ones, which indicates that the redox cycles between Cu$^{2+}$/Cu$^+$ and Ce$^{3+}$/Ce$^{4+}$ are more facile to occur in Ce(III)Cu$x$ than in Ce(IV)Cu$x$.

### 3.4. Reduction properties of CuO-CeO$_2$ catalysts (H$_2$-TPR, in situ CO-IR)

#### 3.4.1. H$_2$-TPR results

Fig. 9(a) displays the H$_2$-TPR profiles of Ce(III)Cu$x$ samples. One peak appears at 491 °C in Ce(III)Cu0, belonging to the reduction of surface oxygen species [15], and the other peak at higher temperature is not included here. Ce(III)Cu5 and Ce(III)Cu15 exhibit two reductive peaks (denoted as α and β), which are attributed to the reduction of well dispersed copper species and copper incorporated into CeO$_2$ lattice, respectively [23]. For Ce(III)Cu50 sample, a new reduction peak γ at about 185 °C appears, corresponding to the reduction of crystalline CuO [34]. For Ce(III)Cu30 sample, due to the appearance of a small amount of crystalline CuO detected in XRD pattern, the reduction peak at 168 °C is considered partially from the contribution of crystalline CuO. Accordingly, this peak is nominated as peak δ, which is the overlap of peak β and γ. With the increase of Cu content, the temperatures of peak α decrease from 181 °C to 138 °C, and for peak β the temperatures decrease from 217 °C to 164 °C, which is probably due to that the increase of Cu–O–Ce species with Cu contents facilitates the reduction of copper species by considering the reducibility of Cu–O–Ce species [35]. Furthermore, H$_2$ consumption during the reduction still surpasses the one needed for complete Cu$^{2+}$ to Cu$^0$ reduction (Table 1), which is associated with the concurrent reduction of copper species and CeO$_2$ surface oxygen. As pointed out by Martínez-Arias et al. [10,36], CeO$_2$ reduction can enhance the reducibility of dispersed CuO. Thus, the reduction of cerium entity promotes the reduction of copper species, leading to lower reduction temperature. Besides, for Ce(III)Cu50 sample the actual amount of H$_2$ consumption is
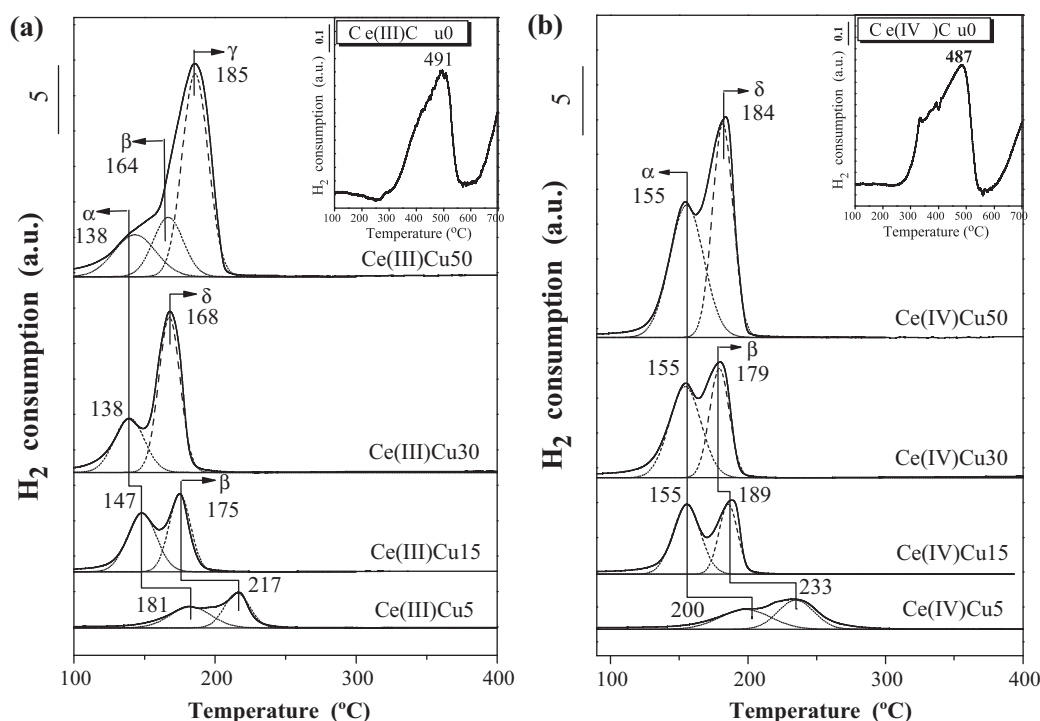
Fig. 9. $H_2$-TPR profiles of CuO-CeO$_2$ catalysts with different Cu contents: (a) Ce(III)Cu$x$; (b) Ce(IV)Cu$x$.

approximate to the theoretical amount of $H_2$ consumption, which implies that the reduction of CeO$_2$ surface oxygen species is hindered due to the covering from excess crystalline CuO.

Fig. 9(b) is the $H_2$-TPR profiles of Ce(IV)Cu$x$ samples. For Ce(IV)Cu0 sample, the peak at 487 °C is ascribed to the reduction of CeO$_2$. When Cu contents are 5, 15 and 30 mol%, peak $\alpha$ and $\beta$ can be observed. For Ce(IV)Cu50 sample, the reduction peak $\delta$ at 184 °C appears. Peak $\alpha$ moves from 200 °C to 155 °C in Ce(IV)Cu5 and Ce(IV)Cu15, and keeps at 155 °C even when Cu content increases continually. Meanwhile, peak $\beta$ shifts to lower temperature gradually with the increase of Cu content. The actual amount of $H_2$ consumption is still larger than the theoretical amount of $H_2$ consumption for this series of CuO-CeO$_2$ samples (Table 1), which indicates the reduction of surface oxygen species of ceria is involved. Additionally, the actual amount of $H_2$ consumption gradually approaches the theoretical amount of $H_2$ consumption with high Cu content (Ce(IV)Cu50), indicating the block of the surface oxygen species of ceria from crystalline CuO.

Compared $H_2$-TPR results of the two series of samples, it can be observed that the reduction temperatures of $\alpha$ and $\beta$ for Ce(III)Cu$x$ samples are lower than those for Ce(IV)Cu$x$ samples with the same Cu contents, implying that the reduction occurs more easily in Ce(III)Cu$x$ than in Ce(IV)Cu$x$. As demonstrated by XPS results, the redox cycles between Cu$^{2+}$/Cu$^+$ and Ce$^{3+}$/Ce$^{4+}$ are more facile to occur in Ce(III)Cu$x$ than in Ce(IV)Cu$x$ due to more Ce$^{3+}$ in Ce(III)Cu$x$, which subsequently brings a stronger synergistic interaction between copper and ceria species in Ce(III)Cu$x$. According to reference [37], the strong synergistic effect between copper and cerium can facilitate the reduction of CuO-CeO$_2$. Thus, the reduction behavior of Ce(III)Cu$x$ is improved greatly.

### 3.4.2. In situ CO-IR spectra results

To further gain insight into the reduction property of the catalysts, in situ FT-IR of CO adsorption was measured in a TPR procedure, and the results have been shown in Fig. 10. Both of the samples display bands in the highest wavenumber zone corresponding mainly to hydroxyl species. These bands at 3710, 3636

and 3522 cm$^{-1}$ are attributed to isolated hydroxyls; additionally, associated hydroxyl species giving a broad band extending from ca. 3800 to 2800 cm$^{-1}$ are detected [38,39]. For Ce(III)Cu15 sample (Fig. 10(a)), the IR band at 2107 cm$^{-1}$, attributed to the linear CO adsorbed on Cu$^+$ sites [40,41], increases gradually from 20 °C, reaches the maximum at 100 °C, and eventually vanishes at 220 °C. The band centered at 2360 cm$^{-1}$ for gaseous CO$_2$ appears at 80 °C, suggesting the incoming CO reduces the surface species of oxides. The bands at 2940, 2845, 1510 and 1386 cm$^{-1}$ are different mode assignments of formate, i.e., $\nu_{O-C-O~(asym)} + \delta_{C-H}$, $\nu_{C-H}$, $\nu_{O-C-O~(asym)}$ and $\nu_{O-C-O~(sym)}$ [38,42]. The bands at 1306, 1475, 1359 and 1062 cm$^{-1}$, ascribed to bi- and mono- or poly dentate carbonate [38], are independent of the temperature. Regarding Ce(IV)Cu15 sample (Fig. 10(b)), Cu$^+$–CO species at 2107 cm$^{-1}$ and gaseous CO$_2$ at 2360 cm$^{-1}$ appear simultaneously at 20 °C, and the intensity of IR band for Cu$^+$–CO shows a maximum at 120 °C and a disappearance at 200 °C. Bi- and mono- or poly dentate carbonates, as well as formate species, are also detected at various temperatures from 20 to 240 °C. While the bands at 1615, 1391 and 1045 cm$^{-1}$ are considered as hydrogen–carbonate species [38,43], which are not observed in the IR spectra of Ce(III)Cu15 sample.

It can be noted that there are some differences between Ce(III)Cu15 and Ce(IV)Cu15 catalysts in FT-IR spectra: (1) Cu$^+$ species can be probed by CO at 20–220 °C in Ce(III)Cu15, while in Ce(IV)Cu15 Cu$^+$ can be detected at 20–200 °C, indicating that Cu$^+$ in Ce(III)Cu15 is more stable than that in Ce(IV)Cu15. As discussed above, the Ce(III)-derived sample, containing more Ce$^{3+}$, has greater ability to assist the redox equilibrium Cu$^{2+}$ + Ce$^{3+}$ $\leftrightarrow$ Cu$^+$ + Ce$^{4+}$ in shifting to right to form more stable Cu$^+$ species, which is more difficult for the Ce(IV)-derived sample. (2) Gaseous CO$_2$ (2360 cm$^{-1}$) appears at 80 °C for Ce(III)Cu15 sample, while this species appears at 20 °C for Ce(IV)Cu15. CO$_2$ formation is due to the interaction of CO with Cu$^{2+}$ ions with unsaturated coordination leading to their reduction, while subsequent CO adsorption on reduced centers produces the Cu$^+$-carbonyl species [9]. The relation between gaseous CO$_2$ and Cu$^+$–CO is revealed in Fig. 11. For Ce(III)Cu15 sample, CO$_2$ is not detected from 20 to 60 °C, and the intensities
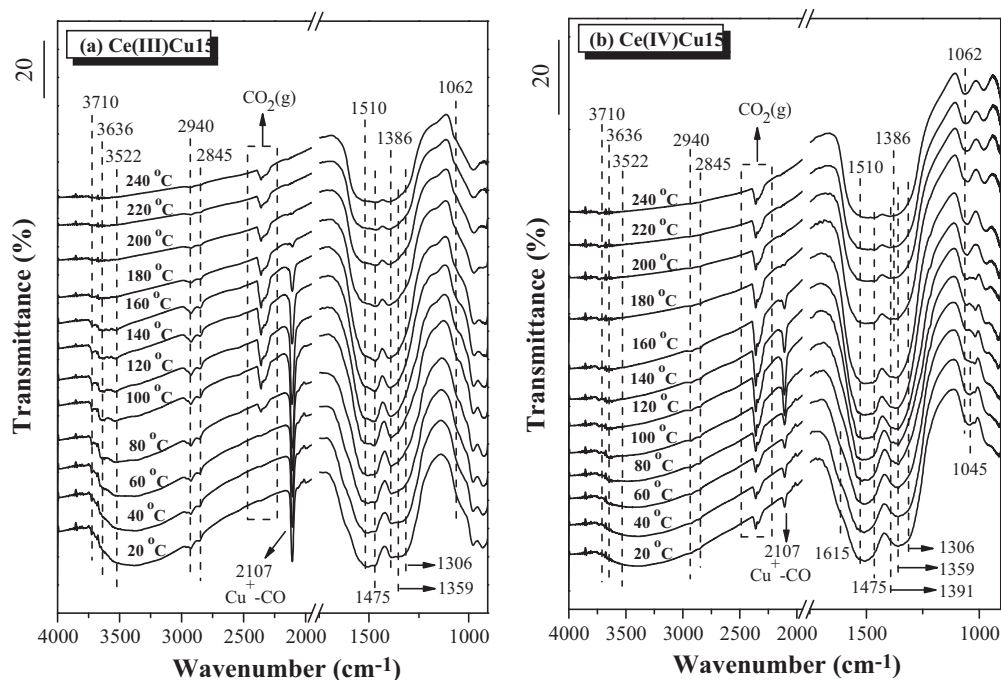
**Fig. 10.** In situ FT-IR spectra of CO adsorption on (a) Ce(III)Cu15; (b) Ce(IV)Cu15.

of $Cu^+$–CO keep the same. As $CO_2$ appears at $80\,°C$, the intensity of $Cu^+$–CO increases. It means that $Cu^+$ is contained in Ce(III)Cu15 sample, and can exist steadily at $20$–$60\,°C$. For Ce(IV)Cu15 sample, the intensities of $CO_2$ elevate gradually with the increase of temperature from $20$ to $60\,°C$, and the intensities of $Cu^+$–CO increase simultaneously. These results indicate that $Cu^+$ is produced by the reduction of $Cu^{2+}$ in Ce(IV)Cu15 sample, accompanying with $CO_2$ appearance. This difference accounts for that the stability of $Cu^+$ is enhanced by electron interaction between $Cu^{2+}/Cu^+$ and $Ce^{3+}/Ce^{4+}$ in Ce(III)-derived sample. (3) Hydrogen–carbonate species can be detected at 1615, 1391 and $1045\,cm^{-1}$ for Ce(IV)Cu15, which are very stable even after heat treatment up to $240\,°C$. However, these carbonates are not observed for Ce(III)Cu15. Carbonates absorbed on the catalyst surface can prevent the $Ce^{3+}/Ce^{4+}$ redox interplay at

the copper–cerium interface and poison active sites of the catalyst [44,45], which is adverse for the activity.

### 3.5. Catalytic tests of CO oxidation

Fig. 12 shows turnover frequency (TOF, $s^{-1}$) of CO over per copper atom as a function of temperature for CO oxidation reaction over these $CuO$-$CeO_2$ catalysts. For Ce(III)Cu$x$ samples, the TOF follows the order of Ce(III)Cu15 > Ce(III)Cu5 > Ce(III)Cu30 > Ce(III)Cu50. For Ce(IV)Cu$x$ ones, the order is ranked as Ce(IV)Cu15 > Ce(IV)Cu30 > Ce(IV)Cu5 > Ce(IV)Cu50. The catalysts
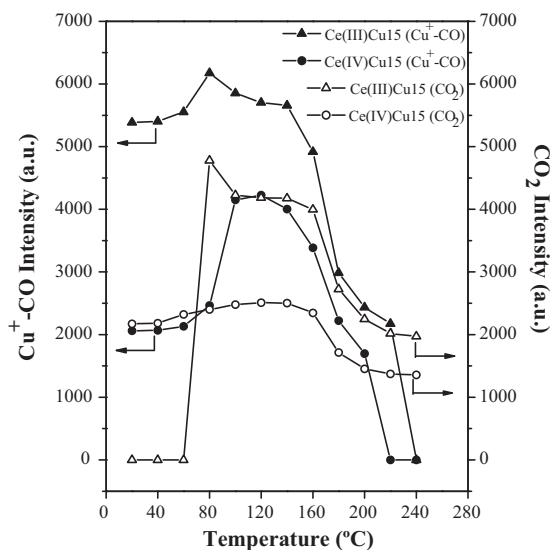


**Fig. 11.** Integrated intensity of IR spectra for $Cu^+$–CO and gaseous $CO_2$ over CuO-CeO$_2$ catalysts as a function of temperature.
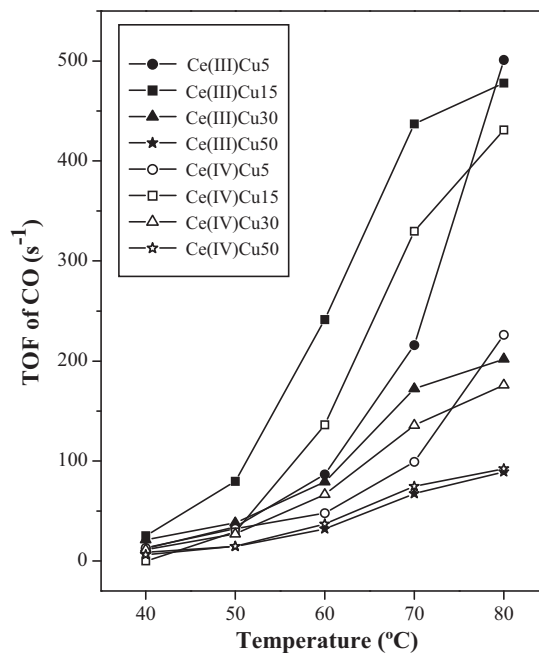


**Fig. 12.** Turnover frequency (TOF, $s^{-1}$) of CO over per copper atom in these CuO-CeO$_2$ catalysts as a function of temperature.
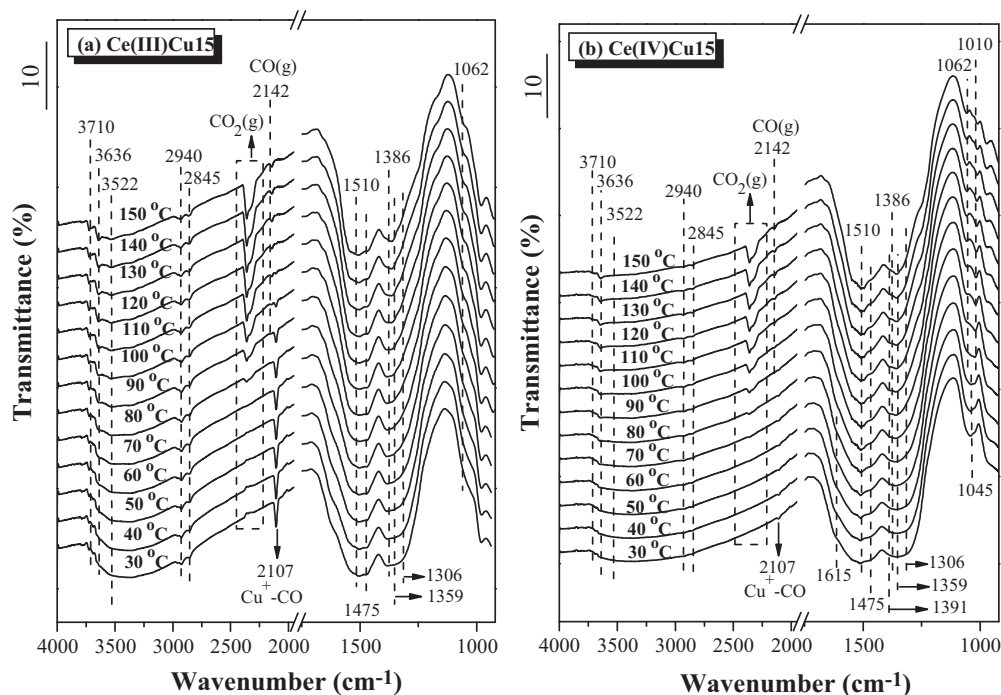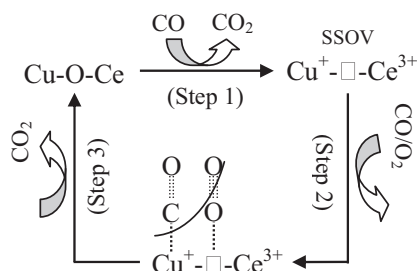
**Fig. 13.** In situ FT-IR spectra of CO and $O_2$ co-adsorption on (a) Ce(III)Cu15; (b) Ce(IV)Cu15.

without detected crystalline CuO display better performance than the catalysts containing crystalline CuO, due to the suppression of surface active species by crystalline CuO [10]. According to the results of structure characterization, Ce(IV)Cux catalysts possess higher surface area and smaller pore size than Ce(III)Cux ones, but the catalytic activities of Ce(IV)Cux are not improved obviously compared with the corresponding Ce(III)Cux ones. In this sense, the surface area and the pore size of catalysts are not the main factors influencing the activity. On the other hand, Ce(III)Cux catalysts exhibit excellent reduction property with low reduction temperatures in $H_2$-TPR and highly stable $Cu^+$ species in CO-IR, which are originated from the enhanced copper–cerium synergic effect due to high concentration of oxygen vacancies and $Ce^{3+}$. As Martínez-Arias et al. [36,46] reported, the reaction mechanism of CO oxidation for $CuO-CeO_2$ catalyst is proposed to involve reductive and oxidative single steps, and the rate-determining one is attributed to the oxidative process. However, the oxidative process depends on the starting degree of reduction attained by the system. In other words, if the system attains a relatively high reduction degree, oxidation of the system can occur sequentially with the ceria component becoming oxidized most preferentially [7]. Accordingly, the catalyst which is more easily to be reduced can exhibit higher reaction activity. Besides, Ce(III)Cux catalysts own stable $Cu^+$ species and high concentration of oxygen vacancies, which provide stable sites for CO chemisorption and active oxygen for reaction to enhance activities. Thus, the different synergistic interactions between Cu and Ce leading to different reduction properties are the main factors influencing the CO oxidation activity. According to our previous study [47], the role of synergistic interaction between copper and ceria in this reaction is tentatively proposed as follows (Scheme 1): considering the reducibility of Cu–O–Ce species [35], the surface Cu–O–Ce species could be reduced by CO in the mixed atmosphere to form surface synergetic oxygen vacancy (SSOV) (i.e. Cu–□–Ce species), accompanying by an exposed $Cu^+$ and a neighboring $Ce^{3+}$ (Step 1), and the exposed $Cu^+$ and oxygen vacancy could provide adsorbed site for CO and activated site for $O_2$, respectively (Step 2). Then the active oxygen reacts facilely with the adsorbed CO species to form $CO_2$ (Step 3).

### 3.6. CO and $O_2$ co-adsorption in situ FT-IR spectra results

In order to further probe the surface species and investigate the influencing factors of the CO oxidation activity, CO and $O_2$ co-adsorption in situ FT-IR spectra of Ce(III)Cu15 and Ce(IV)Cu15 samples were recorded, as shown in Fig. 13. Hydroxyl species can be detected in the range from ca. 4000 to 2800 $cm^{-1}$ [38]. The two rotational branches, centered at ca. 2360 $cm^{-1}$, and a band at 2142 $cm^{-1}$ are corresponding to gaseous $CO_2$ and CO, respectively [48]. The band at 2107 $cm^{-1}$ is observed already upon first contact of the copper-containing samples with CO at room temperature and can be ascribed to $Cu^+$-carbonyl species in accordance with previous works [40,49]. Similar IR spectra at 1600–1000 $cm^{-1}$ assignable to bi- and mono- or poly dentate carbonates, as well as formate species [38,42], are clearly seen over Ce(III)Cu15 and Ce(IV)Cu15 samples, which seem to be independent of temperature. New bands at ca. 1615, 1391, 1045 and 1010 $cm^{-1}$ for hydrogen–carbonate and bidentate carbonates can be distinguished in the IR spectra of Ce(IV)Cu15 sample [9,39]. These chemisorbed carbonates are very stable even after heating to 150 °C.

More important information can be obtained from the comparison of the stability of copper carbonyl and adsorbed carbonate species. It is well recognized that the chemisorption of CO on copper species is important for CO oxidation reaction [14]. Although



**Scheme 1.** The proposed reaction mechanism of CO oxidation over $CuO-CeO_2$ catalysts.

the band for $Cu^+$–CO appears at room temperature for both of the samples, this band intensity of Ce(III)Cu15 is much higher than that of Ce(IV)Cu15. The respective intensities of these $Cu^+$-carbonyls provide a measure of the potential of each catalyst to become interfacially reduced upon interaction of CO with its copper oxide entities, whereas the level of reduction attained in each case is in turn related to the amount of sites available for oxygen to react and close the catalytic cycle [50]. In this sense, the CO oxidation activity is proportional to the intensity of the $Cu^+$-carbonyl band. It is consistent with the results of catalytic tests that Ce(III)Cu15 exhibits higher activity than Ce(IV)Cu15. Moreover, the feature of $Cu^+$–CO disappears at 110 °C for Ce(IV)Cu15 sample, while for Ce(III)Cu15 sample, the desorption process is very slow and this feature still remains at 150 °C. The difference in decomposition of $Cu^+$–CO species between Ce(III)Cu15 and Ce(IV)Cu15 implies that CuO-CeO$_2$ catalyst obtained from trivalent ceric precursor has the potential to facilitate the redox equilibrium of $Cu^{2+} + Ce^{3+} \leftrightarrow Cu^+ + Ce^{4+}$ shifting to right and the stabilization of $Cu^+$ on the surface, which is beneficial for the enhancement of CO oxidation activity. Apart from the above discussion, it is found that the adsorbed hydrogen–carbonate species over Ce(IV)Cu15, which are not observed on Ce(III)Cu15, are difficult to decompose. Active sites can be blocked by carbonate species, resulting in surface poisoning [49]. It is reasonable that the carbonate species would limit reaction rates and lead to low activity of Ce(IV)Cu15 [51].

## 4. Conclusions

As demonstrated by comprehensive characterizations, the use of different cerium precursors leads to different properties of mesoporous CuO-CeO$_2$ catalysts: (1) the use of $(NH_4)_2Ce(NO_3)_6$ precursor can improve the surface area, pore size and particle size, instead of elevating the reduction property and catalytic activity. (2) The use of Ce(NO$_3$)$_3$ precursor can promote the redox equilibrium of $Cu^{2+} + Ce^{3+} \leftrightarrow Cu^+ + Ce^{4+}$ shifting to right and the formation of high amount of $Cu^+$ species and oxygen vacancies, which are responsible for the improved reducibility and activity for CO oxidation. (3) Ce(III)-derived samples contain high amount of $Ce^{3+}$, leading to facile $Ce^{4+}/Ce^{3+}$ redox cycle and meanwhile promotion of copper species reduction. (4) Ce(IV)-derived samples are prone to adsorb carbonate species, which is adverse for the activity of CO oxidation.

## Acknowledgments

## References

[1] M. Kang, M.W. Song, C.H. Lee, Appl. Catal. A: Gen. 251 (2003) 143–156.
[2] X.L. Tang, B.C. Zhang, Y. Li, Y.D. Xu, Q. Xin, W.J. Shen, Appl. Catal. A: Gen. 288 (2005) 116–125.
[3] H.Q. Zhu, Z.F. Qin, W.J. Shan, W.J. Shen, J.G. Wang, J. Catal. 225 (2004) 267–277.
[4] F. Mariño, C. Descorme, D. Duprez, Appl. Catal. B: Environ. 54 (2004) 59–66.
[5] Q. Fu, A. Weber, M. Flytzani-Stephanopoulos, Catal. Lett. 77 (2001) 87–95.
[6] J.B. Wang, D.H. Tsai, T.J. Huang, J. Catal. 208 (2002) 370–380.
[7] A. Martínez-Arias, A.B. Hungría, M. Fernández-García, J.C. Conesa, G. Munuera, J. Phys. Chem. B 108 (2004) 17983–17991.
[8] W. Liu, M. Flytzani-Stephanopoulos, J. Catal. 153 (1995) 304–316.
[9] A. Martínez-Arias, M. Fernández-García, J. Soria, J.C. Conesa, J. Catal. 182 (1999) 367–377.
[10] B. Skårman, D. Grandjean, R.E. Benfield, A. Hinz, A. Andersson, L.R. Wallenberg, J. Catal. 211 (2002) 119–133.
[11] A. Martínez-Arias, A.B. Hungría, G. Munuera, D. Gamarra, Appl. Catal. B: Environ. 65 (2006) 207–216.
[12] G. Sedmak, S. Hočevar, J. Levec, J. Catal. 222 (2004) 87–99.
[13] H.B. Zou, X.F. Dong, W.M. Lin, Appl. Surf. Sci. 253 (2006) 2893–2898.
[14] Z.Y. Pu, X.S. Liu, A.P. Jia, Y.L. Xie, J.Q. Lu, M.F. Luo, J. Phys. Chem. C 112 (2008) 15045–15051.
[15] M.F. Luo, Y.P. Song, J.Q. Lu, X.Y. Wang, Z.Y. Pu, J. Phys. Chem. C 111 (2007) 12686–12692.
[16] W.H. Shen, X.P. Dong, Y.F. Zhu, H.R. Chen, J.L. Shi, Microporous Mesoporous Mater. 85 (2005) 157–162.
[17] S. Bernal, J.J. Calvino, M.A. Cauqui, J.M. Gatica, C. Larese, J.A. Pérez Omil, J.M. Pintado, Catal. Today 50 (1999) 175–206.
[18] X.L. Tang, B.C. Zhang, Y. Li, Y.D. Xu, Q. Xin, W.J. Shen, Catal. Today 93–95 (2004) 191–198.
[19] Y. Li, Q. Fu, M. Flytzani-Stephanopoulos, Appl. Catal. B: Environ. 27 (2000) 179–191.
[20] B.M. Reddy, P. Lakshmanan, A. Khan, S. Loridant, C. López-Cartes, T.C. Rojas, A. Fernández, J. Phys. Chem. B 109 (2005) 13545–13552.
[21] J.L. Cao, Y. Wang, X.L. Yu, S.R. Wang, S.H. Wu, Z.Y. Yuan, Appl. Catal. B: Environ. 79 (2008) 26–34.
[22] S. Letichevsky, C.A. Tellez, R.R. de Avillez, M.I.P. da Silva, M.A. Fraga, L.G. Appel, Appl. Catal. B: Environ. 58 (2005) 203–210.
[23] M.F. Luo, J.M. Ma, J.Q. Lu, Y.P. Song, Y.J. Wang, J. Catal. 246 (2007) 52–59.
[24] W.J. Shan, W.J. Shen, C. Li, Chem. Mater. 15 (2003) 4761–4767.
[25] W.D. Cai, F. Chen, X.X. Shen, L.J. Chen, J.L. Zhang, Appl. Catal. B: Environ. 101 (2010) 160–168.
[26] R. Kydd, W.Y. Teoh, K. Wong, Y. Wang, J. Scott, Q.H. Zeng, A.B. Yu, J. Zou, R. Amal, Adv. Funct. Mater. 19 (2009) 369–377.
[27] J.E. Spanier, R.D. Robinson, F. Zhang, S.W. Chan, I.P. Herman, Phys. Rev. B 64 (2001) 245407–245411.
[28] M. Fernández-García, A. Martínez-Arias, J.C. Hanson, J.A. Rodriguez, Chem. Rev. 104 (2004) 4063–4104.
[29] L. Ilieva, G. Pantaleo, I. Ivanov, A.M. Venezia, D. Andreeva, Appl. Catal. B: Environ. 65 (2006) 101–109.
[30] L.J. Liu, Z.J. Yao, B. Liu, L. Dong, J. Catal. 275 (2010) 45–60.
[31] J. Silvestre-Albero, F. Rodríguez-Reinose, A. Sepúlveda-Escribano, J. Catal. 210 (2002) 127–136.
[32] B. Wen, M.Y. He, Appl. Catal. B: Environ. 37 (2002) 75–82.
[33] I. Platzman, R. Brener, H. Haick, R. Tannenbaum, J. Phys. Chem. C 112 (2008) 1101–1108.
[34] D. Delimaris, T. Ioannides, Appl. Catal. B: Environ. 89 (2009) 295–302.
[35] P. Bera, K.R. Priolkar, P.R. Sarode, M.S. Hegde, S. Emura, R. Kumashiro, N.P. Lalla, Chem. Mater. 14 (2002) 3591–3601.
[36] A. Martínez-Arias, M. Fernández-García, O. Gálvez, J.M. Coronado, J.A. Anderson, J.C. Conesa, J. Soria, G. Munuera, J. Catal. 195 (2000) 207–216.
[37] W.J. Shan, Z.C. Feng, Z.L. Li, J. Zhang, W.J. Shen, C. Li, J. Catal. 228 (2004) 206–217.
[38] P. Bera, A.L. Cámara, A. Hornés, A. Martínez-Arias, J. Phys. Chem. C 113 (2009) 10689–10695.
[39] A. Holmgren, B. Andersson, D. Duprez, Appl. Catal. B: Environ. 22 (1999) 215–230.
[40] H.Q. Wan, Z. Wang, J. Zhu, X.W. Li, B. Liu, F. Gao, L. Dong, Y. Chen, Appl. Catal. B: Environ. 79 (2008) 254–261.
[41] O. Dulaurent, X. Courtois, V. Perrichon, D. Bianchi, J. Phys. Chem. B 104 (2000) 6001–6011.
[42] A. Hornés, P. Bera, A.L. Cámara, D. Gamarra, G. Munuera, A. Martínez-Arias, J. Catal. 268 (2009) 367–375.
[43] C. Binet, M. Daturi, J.C. Lavalley, Catal. Today 50 (1999) 207–225.
[44] C.V. Ovensen, P. Stolze, J.K. Nørskov, C.T. Campbell, J. Catal. 134 (1992) 445–468.
[45] C.H. Kim, L.T. Thompson, J. Catal. 230 (2005) 66–74.
[46] K. Qian, W.X. Huang, J. Fang, S.S. Lv, B. He, Z.Q. Jiang, S.Q. Wei, J. Catal. 255 (2008) 269–278.
[47] D. Li, Q. Yu, S.S. Li, H.Q. Wan, L.J. Liu, L. Qi, B. Liu, F. Gao, L. Dong, Y. Chen, Chem. Eur. J. 17 (2011) 5668–5679.
[48] F. Morales, E. de Smit, F.M.F. de Groot, T. Visser, B.M. Weckhuysen, J. Catal. 246 (2007) 91–99.
[49] F.C. Meunier, D. Tibiletti, A. Goguet, D. Reid, R. Burch, Appl. Catal. A: Gen. 289 (2005) 104–112.
[50] D. Gamarra, C. Belver, M. Fernández-García, A. Martínez-Arias, J. Am. Chem. Soc. 129 (2007) 12064–12065.
[51] S. Hilaire, X. Wang, T. Luo, R.J. Gorte, J. Wagner, Appl. Catal. A: Gen. 215 (2001) 271–278.